Title

Precision Control of Amphoteric Doping in Cu x Bi2Se3 Nanoplates.

Journal

Precision Chemistry, 2(8)

Authors

Ren, Huaying
Zhou, Jingxuan
Zhang, Ao
et al.

Publication Date

2024-08-26

DOI

10.1021/prechem.4c00046

ACS Partner Journal
PRECISION CHEMISTRY
Editors' Choice
Open Access

pubs.acs.org/PrecisionChem
Article

Precision Control of Amphoteric Doping in $Cu_xBi_2Se_3$ Nanoplates

Huaying Ren, Jingxuan Zhou, Ao Zhang, Zixi Wu, Jin Cai, Xiaoyang Fu, Jingyuan Zhou, Zhong Wan, Boxuan Zhou, Yu Huang, and Xiangfeng Duan*

Cite This: *Precis. Chem.* 2024, 2, 421−427

Read Online

ACCESS | Metrics & More | Article Recommendations | Supporting Information

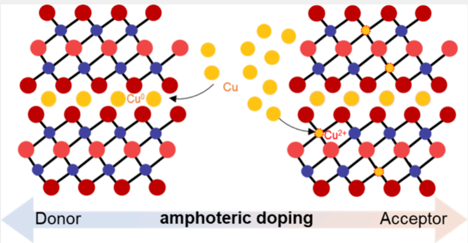

ABSTRACT: Copper-doped Bi_2Se_3 ($Cu_xBi_2Se_3$) is of considerable interest for tailoring its electronic properties and inducing exotic charge correlations while retaining the unique Dirac surface states. However, the copper dopants in $Cu_xBi_2Se_3$ display complex electronic behaviors and may function as either electron donors or acceptors depending on their concentration and atomic sites within the Bi_2Se_3 crystal lattice. Thus, a precise understanding and control of the doping concentration and sites is of both fundamental and practical significance. Herein, we report a solution-based one-pot synthesis of $Cu_xBi_2Se_3$ nanoplates with systematically tunable Cu doping concentrations and doping sites. Our studies reveal a gradual evolution from intercalative sites to substitutional sites with increasing Cu concentrations. The Cu atoms at intercalative sites function as electron donors while those at the substitutional sites function as electron acceptors, producing distinct effects on the electronic properties of the resulting materials. We further show that $Cu_{0.18}Bi_2Se_3$ exhibits superconducting behavior, which is not present in Bi_2Se_3, highlighting the essential role of Cu doping in tailoring exotic quantum properties. This study establishes an efficient methodology for precise synthesis of $Cu_xBi_2Se_3$ with tailored doping concentrations, doping sites, and electronic properties.

KEYWORDS: *$Cu_xBi_2Se_3$, nanoplates, amphoteric doping, solution-based synthesis, doping sites, conducting thin film, superconductivity*

1. INTRODUCTION

Over the past decades, considerable research efforts have been devoted to two-dimensional layered materials possessing unique Dirac surface states, such as Bi_2Te_3, Sb_2Te_3, and Bi_2Se_3.[1−4] Heteroatom doping in these materials can systematically modulate their electronic properties and/or induce unusual charge correlations.[5−9] For example, copper doping in $Cu_xBi_2Se_3$ plays a dual role in modifying the electronic properties. In particular, the $Cu^{+/0}$ atoms intercalated in the Bi_2Se_3 van der Waals (vdW) gaps typically act as electron donors to enhance the conductivity, while substitutional doped Cu^{2+} ions within the Bi_2Se_3 lattice (occupying Bi^{3+} sites) behave as acceptors to reduce the concentration of free electrons.[10−12] It has also been shown that Cu-doped $Cu_xBi_2Se_3$ may exhibit superconductivity under a certain doping concentration, offering an interesting system for exploring novel phenomena such as odd-parity nematic superconductivity.[9,13,14] Specifically, Bi_2Se_3 is a topological insulator with strong spin−orbit coupling (SOC) and is characterized by topological invariants of the valence band. Therefore, $Cu_xBi_2Se_3$ holds significant promise for realizing topological superconductivity, a phenomenon that may lead to new physics with important implications for fault-tolerant topological quantum computing.[9,15−18] However, studies to date indicate that superconductivity is detectable only in the range of $0.1 \leq x \leq 0.5$ for $Cu_xBi_2Se_3$, suggesting that the exact doping range can profoundly affect the transport properties of $Cu_xBi_2Se_3$.[19−21] Previous studies also suggested that $Cu_xBi_2Se_3$ maintains the topological surface state while exhibiting superconductivity when $x \leq 0.3$.[5,19,22] Thus, achieving precise control over doping sites and concentration in $Cu_xBi_2Se_3$ is of vital importance for tailoring their electronic and emergent quantum properties.

The current methods for the preparation of $Cu_xBi_2Se_3$ generally involve two strategies: the intercalation of Cu into Bi_2Se_3 and the direct growth of $Cu_xBi_2Se_3$ crystals.[20,21,23−25] Diverse phases of copper precursors, including gaseous, solid, and liquid forms, have been used for intercalating Cu into Bi_2Se_3. Solid-state intercalation could lead to an excess supply of Cu, accompanied by structural alterations in the host lattice.[25] Solution-based chemical and electrochemical intercalation reactions, typically taking place at relatively mild reaction conditions, have also been used for introducing Cu doping in Bi_2Se_3,[21,26] although the slow diffusion in the vdW gaps poses a considerable challenge for scalable preparation of $Cu_xBi_2Se_3$ materials.[21,27,28] The direct growth method, typically involving one-pot self-flux and melt-growth methods, can bypass the solid-state diffusion issue but generally requires

Special Issue: Precision Chemistry for Two-Dimensional Materials

Received: May 28, 2024
Revised: July 10, 2024
Accepted: July 15, 2024
Published: August 4, 2024

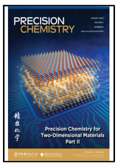

https://doi.org/10.1021/prechem.4c00046

high growth temperatures exceeding 550 °C and a long growth duration of up to several days.[29−31]

Herein, we report a solution-based one-pot synthesis of $Cu_xBi_2Se_3$ nanoplates. By using a Cu precursor (CuI) that gradually releases a low concentration of Cu^+, we successfully synthesized $Cu_xBi_2Se_3$ nanoplates with systematically tailored Cu doping concentrations. Our studies reveal that Cu atoms initially occupy the intercalative sites in vdW gaps at low concentration and gradually occupy Bi substitutional sites with increasing Cu concentration. We further show that intercalative Cu atoms function as electron donors to boost the conductivity and those on the substitutional sites function as electron acceptors to suppress the conductivity. Magnetization measurements reveal the emergence of superconductivity in $Cu_{0.18}Bi_2Se_3$ with a critical temperature (T_c) of approximately 2.4 K, which is absent in pristine Bi_2Se_3, highlighting the essential role of Cu doping in tailoring the exotic quantum properties. This work establishes an efficient method for precise synthesis of $Cu_xBi_2Se_3$ with tailored doping concentration, doping sites, and electronic properties.

2. RESULTS AND DISCUSSION

The preparation of $Cu_xBi_2Se_3$ nanoplates involves a reaction of $Bi(NO_3)_3$ and Na_2SeO_3 in the ethylene glycol (EG) solution with a specific amount of CuI. Bi_2Se_3 exhibits a rhombohedral crystal structure characterized by quintuple layers (QLs) held together by weak vdW interactions (Figure 1a,b). The QLs are composed of alternating planes of Bi and Se atoms arranged in the sequence Se(1)−Bi-Se(2)−Bi-Se(1). The vdW gaps between the QLs provide natural intercalation sites for foreign species, including selected metal atoms such as Cu. At the same time, metal atoms smaller than Bi atoms may also displace Bi atoms from the Bi_2Se_3 QL framework and occupy the Bi substitutional sites and, in extreme cases, entirely replace Bi atoms to form new chalcogenide compounds. Such replacement often occurs under conditions of elevated temperatures and high concentrations of metal ions.[10,20,32,33]

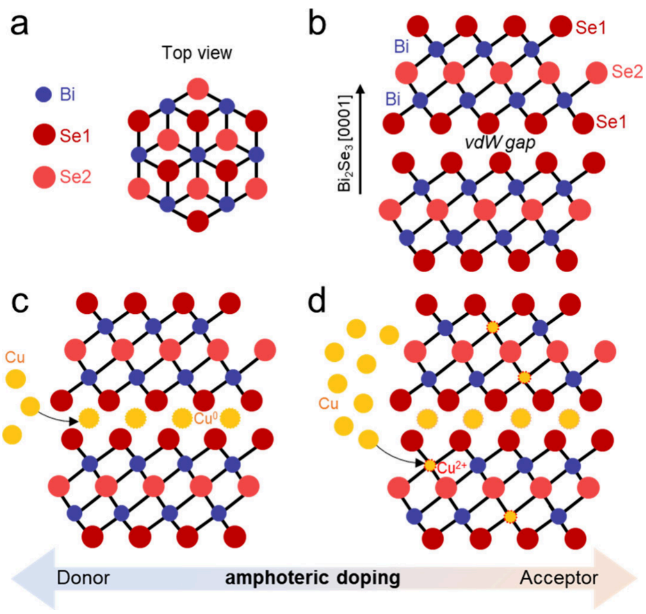

Figure 1. Schematics illustrating the structures of Bi_2Se_3 and $Cu_xBi_2Se_3$ nanoplates synthesized via one-pot synthesis. (a, b) Top and side view of the atomic arrangement of pristine Bi_2Se_3 nanocrystals along with axis [0001]. (c, d) Regulation of copper element occupancy at intercalative and substitutional sites by controlling precursor concentrations.

CuI has a rather low solubility[34] and only exhibits a dynamically equilibrated dilute solution of Cu^+ in EG at a reaction temperature of 195 °C. This solubility limitation presents a unique opportunity for precisely regulating the copper doping concentration in the synthesis of $Cu_xBi_2Se_3$ nanoplates. Cu^+ is expected to readily react to form Cu^0 in EG, according to the positive standard potential (E^0 = +0.52 V).[34−36] Concurrently, the small amount of copper atoms released from the dynamically equilibrated Cu^+ solution is incorporated into the vdW gaps of Bi_2Se_3, forming $Cu_xBi_2Se_3$. In this way, the Cu content between the QLs can be systematically controlled by varying the amount of CuI introduced to the reaction (Figure 1c). The Cu atoms initially occupy the intercalative sites at a low supply of CuI and then compete with Bi for cationic sites within the QL framework at higher CuI feed concentration (Figure 1d). Our studies indicate that it is essential to dehydrate EG to ensure successful Cu doping in $Cu_xBi_2Se_3$. Water contamination could lead to the formation of insoluble Cu_2O precipitates, undermining the incorporation of Cu into Bi_2Se_3 lattice.

Bi_2Se_3, with its inherent lattice symmetry and vdW-layered structure, tends to crystallize in hexagonal nanoplates during the colloidal synthesis process (Figure 2a).[37,38] The $Cu_xBi_2Se_3$ nanoplates also retain the hexagonal nanoplate morphology (Figure 2b). X-ray diffraction (XRD) patterns of all $Cu_xBi_2Se_3$ samples synthesized at varying Cu precursor concentrations exhibit prominent reflections of (00l) peaks (Figure 2a and Figure S1a), indicating the hexagonal nanoplates are generally lying flat on the SiO_2/Si substrate with the [0001] direction

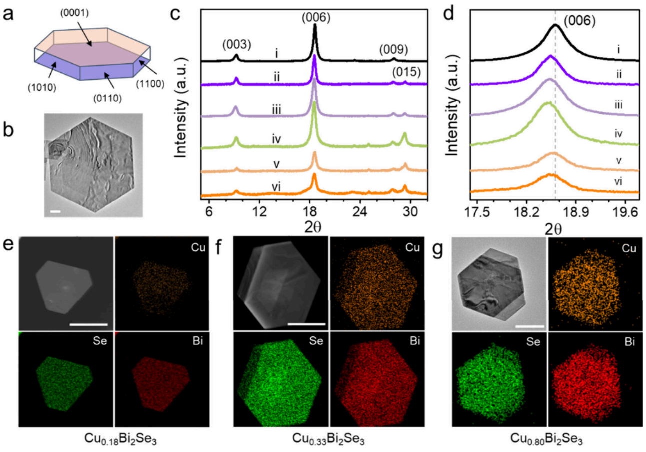

Figure 2. Morphology and structural characterizations. (a) Schematic diagram of the crystal planes for Bi_2Se_3 and $Cu_xBi_2Se_3$ hexagonal nanoplates. (b) TEM image of the $Cu_{0.34}Bi_2Se_3$ nanoplate showing a hexagonal morphology. Scale bar, 200 nm. (c) XRD patterns of Bi_2Se_3 and $Cu_xBi_2Se_3$ nanoplates synthesized at different Cu precursor (CuI) concentrations. Sample i represents the pristine Bi_2Se_3 nanoplates. The Cu precursor concentrations corresponding to samples ii−vi are 0.0014, 0.0025, 0.0045, 0.0090, and 0.0180 mmol/mL, respectively. (d) The enlarged view of XRD patterns shows the (006) peaks in (c). (e−g) STEM and TEM images of $Cu_xBi_2Se_3$ with x = 0.18 (e), 0.33 (f), and 0.80 (g), respectively, and their corresponding EDS elemental mapping images. The nanoplates show hexagonal morphologies. The Cu contents were determined through EDS measurements. Scale bar: 200 nm.

perpendicular to the substrate surface. Overall, the $Cu_xBi_2Se_3$ samples exhibit a structure akin to the pristine $R\bar{3}m$ space group of the Bi_2Se_3 crystal (PDF#00-0012-0732) (Figure S1a), demonstrating the persistence of the layered Bi_2Se_3 framework as the primary structural motif. The enlarged view of the (006) peaks exhibits a minor shift toward lower angles in comparison to pristine Bi_2Se_3 (Figure 2d), indicating a subtle expansion (~0.1 Å) along the direction perpendicular to the QLs in the $Cu_xBi_2Se_3$ samples (Figure S1b), consistent with previous studies.[24,33,39]

The resulting $Cu_xBi_2Se_3$ nanoplates were further characterized using transmission electron microscopy (TEM), scanning TEM (STEM), and energy dispersive X-ray spectroscopy (EDS) with elemental mapping capability. It is confirmed that the hexagonal geometry dominates among the $Cu_xBi_2Se_3$ nanoplates, with lateral dimensions of about 0.2 to 1 μm (Figure 2e−g and Figures S2−S3). Elemental analysis through EDS confirms the presence of Cu, Bi, and Se in the sample synthesized with CuI, wherein the approximate atomic ratio of Bi to Se is roughly 2:3 within instrumental error. The EDS elemental mapping studies reveal the Cu atoms are homogeneously distributed throughout the nanoplates at different Cu doping concentrations (Figure 2e−g and Figures S2−S3). Consistent Cu contents are observed in different nanoplates synthesized under given conditions, indicating a high level of compositional uniformity. Moreover, no iodine was detected within the nanoplates, excluding the possibility of CuI precipitation.

The XPS spectra were further utilized to evaluate the evolution of the Cu content in the $Cu_xBi_2Se_3$ nanoplates grown with different concentrations of Cu precursors (Figure 3a). The relationship between the Cu precursor concentration and the resulting Cu content (x) of $Cu_xBi_2Se_3$, as characterized by XPS, is in Table S1. It is observed that x consistently falls below the Cu:Bi feed ratio, attributed to the low solubility of CuI, resulting in incomplete incorporation of Cu in the $Cu_xBi_2Se_3$ nanoplates. We have further analyzed the evolution of the Cu oxidation state as a function of Cu doping concentration x in $Cu_xBi_2Se_3$. It should be noted that distinguishing between zerovalent copper and Cu(I) by XPS is challenging. Nonetheless, previous studies suggest that both Cu(I) and Cu(0) species positively contribute to the electron concentration, while Cu(II) suppresses the concentration of free electrons.[11,30] Therefore, we have primarily focused on identifying the presence and ratio of Cu(II) as a function of total doping concentration x. Our XPS analysis reveals no Cu(II) is present in the $Cu_xBi_2Se_3$ nanoplates synthesized at low Cu doping concentrations, and Cu(II) species start appearing at higher Cu doping concentrations (Figure 3a). At the same time, it is observed that a Bi:Se atomic ratio of 2:3 is largely maintained at lower Cu doping concentrations, which decreases notably when $x > 0.5$. A plot of Cu(II) ratio and Bi:Se ratio vs doping concentration x reveals a closely correlated evolution of Cu(II) species and Bi:Se ratio with doping concentration x (Figure 3b). As the Cu(II) concentration increases, the Bi:Se ratio decreases, indicating that Cu(II) is associated with substitutional doping of the cationic sites. These analyses demonstrate that Cu atoms largely occupy intercalative sites at low concentrations and begin to take substitutional sites at higher Cu doping concentrations.

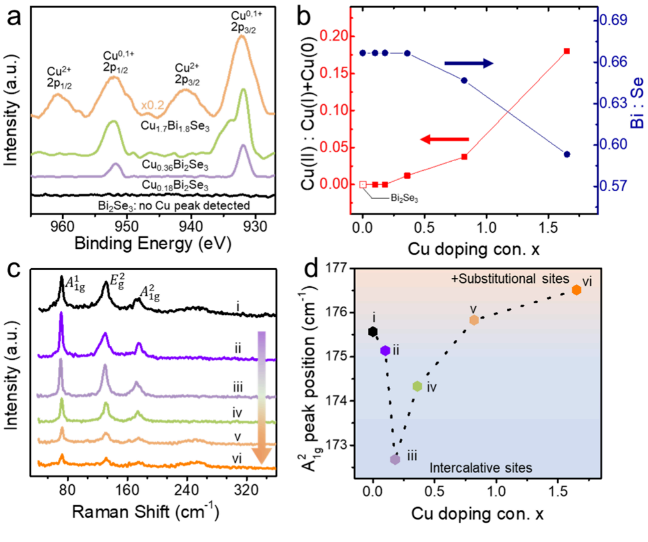

Figure 3. Characterization of Cu contents and doping sites. (a) Cu 2p XPS spectra collected from Bi_2Se_3, $Cu_{0.18}Bi_2Se_3$, $Cu_{0.36}Bi_2Se_3$, and $Cu_{1.7}Bi_{1.8}Se_3$ samples. The original intensity of the $Cu_{1.7}Bi_{1.8}Se_3$ sample has been multiplied by 0.2. (b) The ratio of Cu(II):Cu(I) + Cu(0) (right axis, red solid squares) and the Bi:Se ratio (left axis, blue dots) as a function of Cu doping concentration x in $Cu_xBi_{2-y}Se_3$. The Cu contents were determined through XPS elemental calibration of the corresponding samples. The hollow square represents the intrinsic Bi_2Se_3 sample without copper doping. (c, d) Raman spectra (c) and $A_{1g}{}^2$ peaks shift (d) of Bi_2Se_3 and $Cu_xBi_{2-y}Se_3$ nanoplates of different Cu doping concentrations x. Sample i in (c, d) represents the pristine Bi_2Se_3 nanoplates. The arrow in (c) indicates the direction of increasing Cu doping concentration x.

Raman spectra of Bi_2Se_3 and $Cu_xBi_2Se_3$ nanoplates show three characteristic peaks located at ~71.5, ~131.5, and ~175.5 cm^{-1} (Figure 3c), corresponding to the $A_{1g}{}^1$, $E_g{}^2$, and $A_{1g}{}^2$ vibrational modes of Bi_2Se_3, respectively.[23,40] With increasing Cu doping concentration, it becomes evident that the $E_g{}^2$ peak gradually broadens and the signal-to-noise ratio deteriorates. This phenomenon may be attributed to the transition from the intercalative doping between QLs to the substitutional doping within the QL framework. The $A_{1g}{}^2$ mode of Bi_2Se_3 crystals, corresponding to vibrations of Bi and Se atoms along the c direction, provides a useful measure to evaluate the Cu sites. In brief, the copper atoms occupying intercalative sites weaken the interactions between QLs and shift the $A_{1g}{}^2$ modes toward lower frequencies,[33,39,41] while the substitution of Bi atoms with smaller atoms, such as Cu, strengthens the interlayer vdW interactions and leads to a blue shift of the Raman peaks ($A_{1g}{}^1$, $E_g{}^2$, and $A_{1g}{}^2$). Analysis of the peak position evolution with Cu precursor concentrations (Figure 3d and Figure S4a−g) reveals an initial redshift followed by a subsequent blue shift, suggesting that Cu atoms initially occupy the intercalative sites between the QLs and progressively substitute Bi atoms in QLs at higher Cu doping concentrations. An even further increase in Cu content exacerbates such cationic substitution, leading to gradual disruption of the original Bi_2Se_3 crystal structure, ultimately resulting in the formation of $Cu_{2-x}Se$ (Figure S5).

These analyses demonstrate that the position occupied by Cu can be controllable by tailoring the precursor concentrations. Such precise control is critical for tailoring their electronic properties, since the different sites have an entirely opposite effect, with intercalative Cu functioning as an electron donor and substitutional Cu functioning as an acceptor. Therefore, understanding the concentration of Cu and its

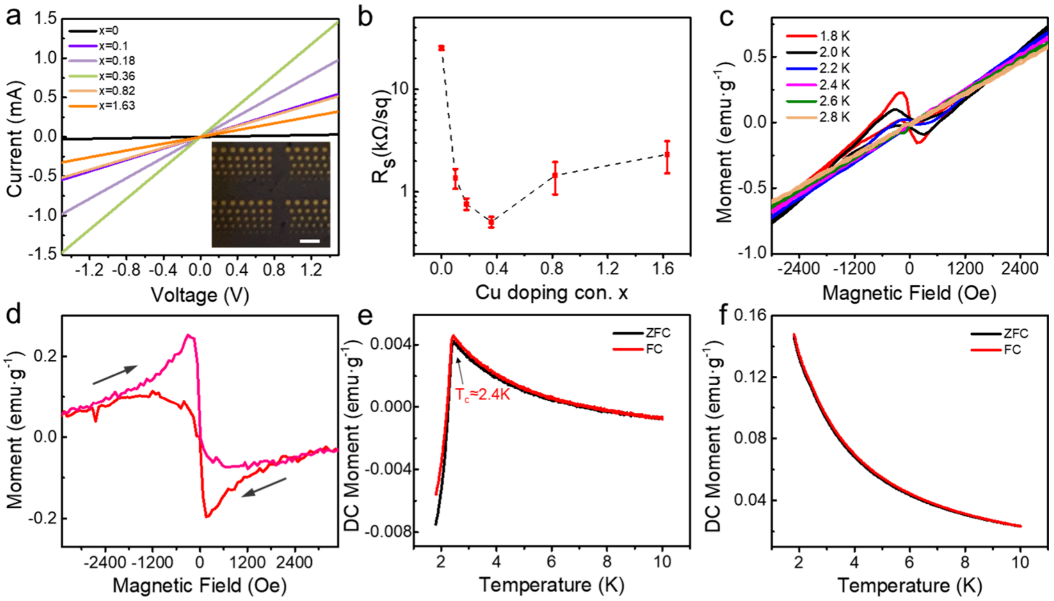

Figure 4. Electrical and magnetic characterization. (a) $I-V$ curves of the Bi_2Se_3 and $Cu_xBi_2Se_3$ nanoplate thin films with Cu doping concentration x = 0.1, 0.18, 0.36, 0.82, and 1.63. The inset shows a photo of the gold electrode array on the $Cu_xBi_2Se_3$ nanoplate thin film, situated on a SiO_2/Si substrate, used for probing electrical transport properties, scale bar 1 mm. The largest circular electrodes have a diameter of 240 μm and a center-to-center distance of 480 μm. (b) Sheet resistances of the $Cu_xBi_2Se_3$ nanoplate thin films as a function of Cu doping concentrations. (c) Magnetization as a function of applied magnetic field (M−H curves) for $Cu_{0.18}Bi_2Se_3$ nanoplates measured at different temperatures ranging from 1.8 to 2.8 K. (d) The baseline corrected expanded low-field part of the magnetization curves for $Cu_{0.18}Bi_2Se_3$ nanoplates at 1.8 K. Two arrows indicate the direction of increasing magnetic field for the upper and lower curves, respectively. (e, f) Temperature dependence of magnetization (M−T curve) for $Cu_{0.18}Bi_2Se_3$ (e) and Bi_2Se_3 (f) nanoplates obtained under a magnetic field of 50 Oe during zero-field cooling (ZFC) and field cooling (FC) processes.

oxidation state under different growth conditions is essential for controlling the electronic properties and harnessing the superconducting properties of the $Cu_xBi_2Se_3$ nanoplates.

The solution-based synthesis method can readily yield $Cu_xBi_2Se_3$ colloidal nanoplates that can be used as conductive ink for fabricating conducting thin films through a simple spin coating process. The current−voltage ($I-V$) curves of $Cu_xBi_2Se_3$ nanoplate thin films with different x values all show a linear ohmic behavior (Figure 4a). Overall, our measurements show the nanoplate thin film conductivity first increases with Cu doping and reaches a peak at x = 0.36 and then decreases with further increasing in Cu doping (Figure 4b), indicating the complex nature of Cu doping in $Cu_xBi_2Se_3$ due to different doping sites. When x < 0.36, the Cu atoms predominantly occupy the intercalative sites and behave as electron donors to increase electron concentration; when x > 0.36, the Cu atoms progressively take up cationic substitutional sites and behave as electron acceptors to decrease net electron concentration and suppress the conductivity. These transport studies and the amphoteric nature of Cu dopant are largely consistent with XPS and Raman studies discussed above, highlighting precisely tailorable electronic properties depending on the exact doping concentration and doping sites.

We have further evaluated the superconducting properties of the $Cu_xBi_2Se_3$ nanoplates at different Cu doping concentrations. Superconducting material expels magnetic fields when it is cooled below the critical temperature (T_c). Thus, the magnetization measurements can be used to assess superconducting properties and determine T_c without the need of more complex cryogenic transport measurements. The magnetization versus magnetic field (M−H) curves for Bi_2Se_3, $Cu_{0.18}Bi_2Se_3$, and $Cu_{0.82}Bi_{1.94}Se_3$ show distinct behavior depending on the x-value. Specifically, the pristine Bi_2Se_3 nanoplates and $Cu_{0.82}Bi_{1.94}Se_3$ nanoplates exhibit diamagnetic behavior (Figure S6a,b), while the $Cu_{0.18}Bi_2Se_3$ sample displays notable magnetization hysteresis loops at low temperatures (Figure 4c). Subtracting the baseline data obtained at high temperature reveals a butterfly shaped loop (Figure 4d), a key signature consistent with the typical hysteresis loops of superconductors.[8,42,43] The temperature dependent magnetic susceptibility (M−T curve) for $Cu_{0.18}Bi_2Se_3$ nanoplates exhibits a sharp decline in susceptibility at a T_c of ∼2.4 K under both zero-field-cooling (ZFC) and field-cooling (FC) processes (Figure 4e), confirming the emergence of superconductivity in $Cu_{0.18}Bi_2Se_3$ nanoplates.[5,6,21,30] In contrast, no steep decrease in susceptibility can be observed in either ZFC or FC curves for pristine Bi_2Se_3 nanoplates (Figure 4f), indicating that the superconducting properties observed in $Cu_{0.18}Bi_2Se_3$ are not inherent from Bi_2Se_3 but associated with Cu doping.

3. CONCLUSIONS

In conclusion, we have developed a one-pot synthesis method for producing $Cu_xBi_2Se_3$ nanoplates with controllable Cu doping concentrations and doping sites. This controlled synthesis plays a critical role in tailoring and taming the structural and electronic characteristics that sensitively depend on Cu concentration in $Cu_xBi_2Se_3$ nanoplates. Characterizations revealed that Cu atoms initially occupy intercalative sites between QLs before gradually substituting for Bi atoms in the Bi_2Se_3 QLs at increasing Cu concentrations. Electrical transport studies reveal that conductivity of the $Cu_xBi_2Se_3$ thin film first increases with Cu concentration and then decreases with a further increase in Cu concentration, demonstrating the amphoteric doping nature depending on the exact doping concentrations and doping sites. Moreover, the solution synthesized $Cu_{0.18}Bi_2Se_3$ exhibits signatures of superconductivity at low temperature, which is not present in the pristine Bi_2Se_3 nanoplates and $Cu_{0.82}Bi_{1.94}Se_3$ nanoplates, further underscoring the importance of careful control over doping levels to achieve desired electronic properties. The insights gained from this work provide valuable guidance for future research in material synthesis methodologies and the design of innovative electronic devices.

4. METHODS

4.1. Chemicals

All the chemicals were used as received from commercial sources without further purification unless otherwise specified. Copper(I) iodide (CuI, ≥99.5%), bismuth nitrate pentahydrate ($Bi(NO_3)_3 \cdot 5H_2O$, ≥99.9%), sodium selenite (Na_2SeO_3, ≥99%), ethylene glycol (EG), poly(vinylpyrrolidone) (PVP, MW ≈ 40,000), acetone, and isopropanol (IPA) were purchased from Sigma-Aldrich. Molecular sieves 3A beads were purchased from Alfa Aesar.

4.2. Synthesis of $Cu_xBi_2Se_3$ Nanoplates and Post-treatment

EG used in this reaction was pretreated overnight with dried 3A molecular sieves to remove water. 0.2 mmol of $Bi(NO_3)_3 \cdot 5H_2O$ (0.0970 g), 0.3 mmol of Na_2SeO_3 (0.0519 g), and 2 mmol of PVP (0.2223 g) were dissolved in 7 mL of EG. The mixture was sonicated for 5 min and stirred for 15 min in a three-neck flask before being heated to 80 °C. The setup requires the insertion of a thermal couple into the solution to precisely control the solution temperature with a heating mantle. A reflux condenser is placed vertically for reflux. The spare third neck serves as a feed port, through which 3 mL of ethylene glycol solution containing a specific amount of CuI (∼0−0.052 g) is slowly added dropwise. After sealing the feed port, the temperature was raised to 195 °C. The reaction lasted for 3 h, after which the mixture was allowed to cool naturally to room temperature. The obtained black mixture was ∼10 mL. After adding 15 mL of acetone and 15 mL of isopropanol, the new mixture was thoroughly stirred and centrifuged at 12,000 rpm for 10 min. The solid was redispersed with isopropanol, and the centrifugation step was repeated twice. The washed mixture was then dispersed again with isopropanol and centrifuged at 2,500 rpm for about 5 min to remove the precipitated solid containing excess PVP and aggregated crystals from the bottom. The resulting upper layer of black dispersion is the dispersion of $Cu_xBi_2Se_3$ nanoplates. The $Cu_xBi_2Se_3$ nanoplate dispersion needs to undergo further processing according to characterization and application requirements.

4.3. Characterization

The materials were characterized using a variety of analytical techniques. X-ray diffraction (XRD) experiments were conducted using a Panalytical X'Pert Pro X-ray Powder Diffractometer, while Raman spectroscopy was performed with a HORIBA LabRAM Odyssey instrument. Samples for XRD and Raman spectroscopy experiments were prepared by drop casting nanoplate dispersions onto SiO_2/Si substrates. Transmission electron microscopy (Titan TEM FEI with an acceleration voltage of 300 kV) and scanning transmission electron microscopy (STEM) equipped with energy-dispersive X-ray spectroscopy (EDS) analyses (Titan Cubed Themis G2 300; JEOL JEM-ARM300CF S/STEM, accelerating voltage, 300 kV) were employed to characterize the morphology and elemental distribution within nanoplates. TEM and STEM samples were prepared by drop-casting diluted nanoplate dispersions onto Ni mesh to avoid any interference with Cu content measurements. X-ray photoelectron spectroscopy (Kratos AXIS Ultra DLD spectrometer) was employed to characterize the elemental composition of nanoplates and the oxidation states of copper. Calibration of all XPS spectra utilized a C 1s peak positioned at 284.8 eV, with Shirley background fitting applied to all elements within the surveys. Samples for XPS measurements were prepared by centrifugation at 12,000 rpm for 10 min, followed by vacuum drying. The magnetic properties of nanoplates were probed via the superconducting quantum interference device (SQUID) (MPMS V XL, Quantum Design Company) by using a sample holder with high-purity capsules. UV−vis-NIR spectroscopy (Shimadzu 3100 PC) measurements of absorbance were utilized as the criteria to adjust the concentrations of colloidal conductive inks. The transport characteristics of conductive thin films were assessed using a probe station in conjunction with a Keithley source measure unit.

4.4. Cu(II):Cu(I) + Cu(0) Calculations

The total intensity from Cu(II) species is represented in the combination of the signals from the direct photoemission (∼935 eV) and the shaken-up photoemission (∼941 eV). Cu(0) or Cu(I) species direct photoemission is around ∼932 eV. Quantification of the amount of [Cu(I) + Cu(0)] and Cu(II) species can be obtained by the following equation:

$$[\mathrm{Cu(I)} + \mathrm{Cu(0)}]\% = (A_2)/(A_1 + A_2 + B) \times 100$$

$$\mathrm{Cu(II)}\% = (B + A_1)/(A_1 + A_2 + B) \times 100$$

where B is the area of the shakeup peak of Cu(II) and A_1 and A_2 are the areas of the direct peaks of Cu(II) and Cu(0, I) respectively.[44]

4.5. Preparation of Conductive Thin Films

To investigate the electrical conductivity of thin films after coating, dispersions of $Cu_xBi_2Se_3$ nanoplates with varying Cu doping levels were selected. The relatively uniform size distribution of the nanoplates allows for the utilization of UV−vis-NIR spectroscopy absorbance as a criterion for adjusting the concentration of $Cu_xBi_2Se_3$ nanoplates with varying Cu doping concentrations in the conductive ink formulation. SiO_2 (300 nm)/Si slices treated with oxygen plasma (90 W, 8 min) served as the supporting substrate. To ensure uniformity and continuity of the films, the spin coating method was employed at 2000 rpm and repeated three times. Subsequently, the prepared films were placed on quartz boats and annealed at 350 °C for no less than 40 min under ambient pressure, with argon gas serving as the protective atmosphere in a tube furnace. This annealing process effectively removed the surface PVP and facilitated tighter packing between nanoplates, enabling facile electron transfer between different plates. After the annealing process, the films were covered with a shadow mask containing dot-like holes, and the small round Ti/Au (80 nm/20 nm) electrodes were prepared using the E-beam evaporation method. In a series of electrical measurements, we used circular electrodes with a diameter of 240 μm, with a center-to-center distance of 480 μm.

■ ASSOCIATED CONTENT

Supporting Information

The Supporting Information is available free of charge at https://pubs.acs.org/doi/10.1021/prechem.4c00046.

Additional experimental details and methods, including XRD patterns, TEM images, EDS elemental mapping images, Raman spectra, M-H curves, and doping concentration data (PDF)

■ AUTHOR INFORMATION

Corresponding Author

Xiangfeng Duan − *Department of Chemistry and Biochemistry, University of California, Los Angeles, Los Angeles, California 90095, United States; California NanoSystems Institute, University of California, Los Angeles, Los Angeles, California 90095, United States;* orcid.org/0000-0002-4321-6288; Email: xduan@chem.ucla.edu

Authors

Huaying Ren − *Department of Chemistry and Biochemistry, University of California, Los Angeles, Los Angeles, California 90095, United States;* orcid.org/0000-0003-4785-8031

Jingxuan Zhou − *Department of Materials Science and Engineering, University of California, Los Angeles, Los Angeles, California 90095, United States;* orcid.org/0000-0002-6978-0901

Ao Zhang − *Department of Materials Science and Engineering, University of California, Los Angeles, Los Angeles, California 90095, United States*

Zixi Wu − *Department of Chemistry and Biochemistry, University of California, Los Angeles, Los Angeles, California 90095, United States;* orcid.org/0009-0009-2882-1816

Jin Cai − *Department of Materials Science and Engineering, University of California, Los Angeles, Los Angeles, California 90095, United States*

Xiaoyang Fu − *Department of Chemistry and Biochemistry, University of California, Los Angeles, Los Angeles, California 90095, United States*

Jingyuan Zhou − *Department of Chemistry and Biochemistry, University of California, Los Angeles, Los Angeles, California 90095, United States;* orcid.org/0000-0003-0061-219X

Zhong Wan − *Department of Chemistry and Biochemistry, University of California, Los Angeles, Los Angeles, California 90095, United States*

Boxuan Zhou − *Department of Materials Science and Engineering, University of California, Los Angeles, Los Angeles, California 90095, United States*

Yu Huang − *Department of Materials Science and Engineering and California NanoSystems Institute, University of California, Los Angeles, Los Angeles, California 90095, United States;* orcid.org/0000-0003-1793-0741

Complete contact information is available at: https://pubs.acs.org/10.1021/prechem.4c00046

Author Contributions

X.D. conceived the research. H.R. designed the experiments and developed synthetic methods. H.R. and J.X.Z. performed SQUID measurements and data analysis. H.R. and B.Z. performed XRD and Raman characterizations and analyzed the data. A.Z. performed the XPS measurement and data analysis. J.C. and X.F. performed the TEM and STEM characterization. H.R. performed device fabrication, electrical measurements, and data analysis with help from Z.W. Z.X.W. and J.Y.Z. contributed to the discussions and helped analyze the data. Y.H. and X.D. supervised the research. H.R. and X.D. cowrote the manuscript. All authors discussed the results and commented on the manuscript.

Notes

The authors declare no competing financial interest.

■ ACKNOWLEDGMENTS

The authors acknowledge the Electron Imaging Center for NanoMachines at the CNSI and Nanoelectronic Research Facility at the University of California, Los Angeles for technical support. X.D. acknowledges the UCLA California NanoSystem Institute (CNSI) Noble Family Innovation Fund for material preparation and partial support from the National Science Foundation through grant number 2329192 for transport studies and analysis.

■ REFERENCES

(1) Xia, Y.; Qian, D.; Hsieh, D.; Wray, L.; Pal, A.; Lin, H.; Bansil, A.; Grauer, D.; Hor, Y. S.; Cava, R. J.; Hasan, M. Z. Observation of a Large-Gap Topological-Insulator Class with a Single Dirac Cone on the Surface. *Nature Phys.* **2009**, *5* (6), 398−402.

(2) Zhang, Y.; He, K.; Chang, C.-Z.; Song, C.-L.; Wang, L.-L.; Chen, X.; Jia, J.-F.; Fang, Z.; Dai, X.; Shan, W.-Y.; Shen, S.-Q.; Niu, Q.; Qi, X.-L.; Zhang, S.-C.; Ma, X.-C.; Xue, Q.-K. Crossover of the Three-Dimensional Topological Insulator Bi2Se3 to the Two-Dimensional Limit. *Nature Phys.* **2010**, *6* (8), 584−588.

(3) Charpentier, S.; Galletti, L.; Kunakova, G.; Arpaia, R.; Song, Y.; Baghdadi, R.; Wang, S. M.; Kalaboukhov, A.; Olsson, E.; Tafuri, F.; Golubev, D.; Linder, J.; Bauch, T.; Lombardi, F. Induced Unconventional Superconductivity on the Surface States of Bi2Te3 Topological Insulator. *Nat. Commun.* **2017**, *8* (1), 2019.

(4) Zhang, H.; Liu, C.-X.; Qi, X.-L.; Dai, X.; Fang, Z.; Zhang, S.-C. Topological Insulators in Bi2Se3, Bi2Te3 and Sb2Te3 with a Single Dirac Cone on the Surface. *Nature Phys.* **2009**, *5* (6), 438−442.

(5) Hor, Y. S.; Williams, A. J.; Checkelsky, J. G.; Roushan, P.; Seo, J.; Xu, Q.; Zandbergen, H. W.; Yazdani, A.; Ong, N. P.; Cava, R. J. Superconductivity in Cu x Bi 2 Se 3 and Its Implications for Pairing in the Undoped Topological Insulator. *Phys. Rev. Lett.* **2010**, *104* (5), 057001.

(6) Kawai, T.; Wang, C. G.; Kandori, Y.; Honoki, Y.; Matano, K.; Kambe, T.; Zheng, G. Direction and Symmetry Transition of the Vector Order Parameter in Topological Superconductors CuxBi2Se3. *Nat. Commun.* **2020**, *11* (1), 235.

(7) Willa, K.; Willa, R.; Song, K. W.; Gu, G. D.; Schneeloch, J. A.; Zhong, R.; Koshelev, A. E.; Kwok, W.-K.; Welp, U. Nanocalorimetric Evidence for Nematic Superconductivity in the Doped Topological Insulator Sr 0.1 Bi 2 Se 3. *Phys. Rev. B* **2018**, *98* (18), 184509.

(8) Shen, J.; He, W.-Y.; Yuan, N. F. Q.; Huang, Z.; Cho, C.; Lee, S. H.; Hor, Y. S.; Law, K. T.; Lortz, R. Nematic Topological Superconducting Phase in Nb-Doped Bi2Se3. *npj Quant Mater.* **2017**, *2* (1), 59.

(9) Yonezawa, S.; Tajiri, K.; Nakata, S.; Nagai, Y.; Wang, Z.; Segawa, K.; Ando, Y.; Maeno, Y. Thermodynamic Evidence for Nematic Superconductivity in CuxBi2Se3. *Nature Phys.* **2017**, *13* (2), 123−126.

(10) Tanaka, Y.; Nakayama, K.; Souma, S.; Sato, T.; Xu, N.; Zhang, P.; Richard, P.; Ding, H.; Suzuki, Y.; Das, P.; Kadowaki, K.; Takahashi, T. Evolution of Electronic Structure upon Cu Doping in the Topological Insulator Bi 2 Se 3. *Phys. Rev. B* **2012**, *85* (12), 125111.

(11) Vaško, A.; Tichý, L.; Horák, J.; Weissenstein, J. Amphoteric Nature of Copper Impurities in Bi2Se3 Crystals. *Appl. Phys.* **1974**, *5* (3), 217−221.

(12) Liu, Z.; Wei, X.; Wang, J.; Pan, H.; Ji, F.; Xi, F.; Zhang, J.; Hu, T.; Zhang, S.; Jiang, Z.; Wen, W.; Huang, Y.; Ye, M.; Yang, Z.; Qiao, S. Local Structures around 3 d Metal Dopants in Topological Insulator Bi 2 Se 3 Studied by EXAFS Measurements. *Phys. Rev. B* **2014**, *90* (9), 094107.

(13) Tao, R.; Yan, Y.-J.; Liu, X.; Wang, Z.-W.; Ando, Y.; Wang, Q.-H.; Zhang, T.; Feng, D.-L. Direct Visualization of the Nematic Superconductivity in Cu x Bi 2 Se 3. *Phys. Rev. X* **2018**, *8* (4), 041024.

(14) Yokoyama, M.; Nishigaki, H.; Ogawa, S.; Nita, S.; Shiokawa, H.; Matano, K.; Zheng, G. Manipulating the Nematic Director by Magnetic Fields in the Spin-Triplet Superconducting State of Cu x Bi 2 Se 3. *Phys. Rev. B* **2023**, *107* (10), L100505.

(15) Matano, K.; Kriener, M.; Segawa, K.; Ando, Y.; Zheng, G. Spin-Rotation Symmetry Breaking in the Superconducting State of CuxBi2Se3. *Nature Phys.* **2016**, *12* (9), 852−854.

(16) Wang, J.; Ran, K.; Li, S.; Ma, Z.; Bao, S.; Cai, Z.; Zhang, Y.; Nakajima, K.; Ohira-Kawamura, S.; Čermák, P.; Schneidewind, A.; Savrasov, S. Y.; Wan, X.; Wen, J. Evidence for Singular-Phonon-Induced Nematic Superconductivity in a Topological Superconductor Candidate Sr0.1Bi2Se3. *Nat. Commun.* **2019**, *10* (1), 2802.

(17) Wan, Z.; Qiu, G.; Ren, H.; Qian, Q.; Li, Y.; Xu, D.; Zhou, J.; Zhou, B.; Wang, L.; Yang, T.-H.; Sofer, Z.; Huang, Y.; Wang, K. L.;

Duan, X. Unconventional Superconductivity in Chiral Molecule–TaS2 Hybrid Superlattices. *Nature* **2024**, DOI: 10.1038/s41586-024-07625-4.

(18) Frolov, S. M.; Manfra, M. J.; Sau, J. D. Topological Superconductivity in Hybrid Devices. *Nat. Phys.* **2020**, *16* (7), 718–724.

(19) Yonezawa, S. Nematic Superconductivity in Doped Bi2Se3 Topological Superconductors. *Condensed Matter* **2019**, *4* (1), 2.

(20) Li, M.; Wang, Z.; Yang, L.; Li, D.; Yao, Q. R.; Rao, G. H.; Gao, X. P. A.; Zhang, Z. Electron Delocalization and Relaxation Behavior in Cu-Doped B i 2 S e 3 Films. *Phys. Rev. B* **2017**, *96* (7), 075152.

(21) Kriener, M.; Segawa, K.; Ren, Z.; Sasaki, S.; Wada, S.; Kuwabata, S.; Ando, Y. Electrochemical Synthesis and Superconducting Phase Diagram of Cu x Bi 2 Se 3. *Phys. Rev. B* **2011**, *84* (5), 054513.

(22) Wray, L. A.; Xu, S.-Y.; Xia, Y.; Hor, Y. S.; Qian, D.; Fedorov, A. V.; Lin, H.; Bansil, A.; Cava, R. J.; Hasan, M. Z. Observation of Topological Order in a Superconducting Doped Topological Insulator. *Nature Phys.* **2010**, *6* (11), 855–859.

(23) Guo, Y.; Zhou, J.; Liu, Y.; Zhou, X.; Yao, F.; Tan, C.; Wu, J.; Lin, L.; Liu, K.; Liu, Z.; Peng, H. Chemical Intercalation of Topological Insulator Grid Nanostructures for High-Performance Transparent Electrodes. *Adv. Mater.* **2017**, *29* (44), 1703424.

(24) Wang, M.; Al-Dhahir, I.; Appiah, J.; Koski, K. J. Deintercalation of Zero-Valent Metals from Two-Dimensional Layered Chalcogenides. *Chem. Mater.* **2017**, *29* (4), 1650–1655.

(25) Buha, J.; Manna, L. Solid State Intercalation, Deintercalation, and Cation Exchange in Colloidal 2D Bi 2 Se 3 and Bi 2 Te 3 Nanocrystals. *Chem. Mater.* **2017**, *29* (3), 1419–1429.

(26) Koski, K. J.; Cha, J. J.; Reed, B. W.; Wessells, C. D.; Kong, D.; Cui, Y. High-Density Chemical Intercalation of Zero-Valent Copper into Bi 2 Se 3 Nanoribbons. *J. Am. Chem. Soc.* **2012**, *134* (18), 7584–7587.

(27) Wang, Y.; Wang, W.; Sang, D.; Yu, K.; Lin, H.; Qu, F. Cu 2−x Se/Bi 2 Se 3 @PEG Z-Scheme Heterostructure: A Multimode Bioimaging Guided Theranostic Agent with Enhanced Photo/Chemodynamic and Photothermal Therapy. *Biomater. Sci.* **2021**, *9* (12), 4473–4483.

(28) Maclachlan, J. B.; Kruesi, W. H.; Fray, D. J. Intercalation of Copper into Bismuth Telluride. *J. Mater. Sci.* **1992**, *27* (15), 4223–4229.

(29) Schneeloch, J. A.; Zhong, R. D.; Xu, Z. J.; Gu, G. D.; Tranquada, J. M. Dependence of Superconductivity in Cu x Bi 2 Se 3 on Quenching Conditions. *Phys. Rev. B* **2015**, *91* (14), 144506.

(30) Kriener, M.; Segawa, K.; Ren, Z.; Sasaki, S.; Ando, Y. Bulk Superconducting Phase with a Full Energy Gap in the Doped Topological Insulator Cu x Bi 2 Se 3. *Phys. Rev. Lett.* **2011**, *106* (12), 127004.

(31) Li, M. T.; Fang, Y. F.; Zhang, J. C.; Yi, H. M.; Zhou, X. J.; Lin, C. T. Magnetotransport Study of Topological Superconductor Cu 0.10 Bi 2 Se 3 Single Crystal. *J. Phys.: Condens. Matter* **2018**, *30* (12), 125702.

(32) Richter, W.; Becker, C. R. A Raman and Far-infrared Investigation of Phonons in the Rhombohedral V 2 – VI 3 Compounds Bi 2 Te 3, Bi 2 Se 3, Sb 2 Te 3 and Bi 2 (Te 1− x Se x) 3 (0 < *x* < 1), (Bi 1− y Sb y) 2 Te 3 (0 < *y* < 1). *Physica Status Solidi (b)* **1977**, *84* (2), 619–628.

(33) Shetty, P. P.; Kondekar, N.; Thenuwara, A. C.; Boebinger, M. G.; Wright, S. C.; Tian, M.; McDowell, M. T. In Situ Dynamics during Heating of Copper-Intercalated Bismuth Telluride. *Matter* **2020**, *3* (4), 1246–1262.

(34) Gawande, M. B.; Goswami, A.; Felpin, F.-X.; Asefa, T.; Huang, X.; Silva, R.; Zou, X.; Zboril, R.; Varma, R. S. Cu and Cu-Based Nanoparticles: Synthesis and Applications in Catalysis. *Chem. Rev.* **2016**, *116* (6), 3722–3811.

(35) Morelock, C. R.; Sears, G. W. Growth Mechanism of Copper Whiskers by Hydrogen Reduction of Cuprous Iodide. *J. Chem. Phys.* **1959**, *31* (4), 926–928.

(36) Teichert, J.; Doert, T.; Ruck, M. Mechanisms of the Polyol Reduction of Copper(ii) Salts Depending on the Anion Type and Diol Chain Length. *Dalton Trans.* **2018**, *47* (39), 14085–14093.

(37) Soni, A.; Yanyuan, Z.; Ligen, Y.; Aik, M. K. K.; Dresselhaus, M. S.; Xiong, Q. Enhanced Thermoelectric Properties of Solution Grown Bi 2 Te 3− x Se x Nanoplatelet Composites. *Nano Lett.* **2012**, *12* (3), 1203–1209.

(38) Lin, Z.; Chen, Y.; Yin, A.; He, Q.; Huang, X.; Xu, Y.; Liu, Y.; Zhong, X.; Huang, Y.; Duan, X. Solution Processable Colloidal Nanoplates as Building Blocks for High-Performance Electronic Thin Films on Flexible Substrates. *Nano Lett.* **2014**, *14* (11), 6547–6553.

(39) Chen, H.-J.; Wu, K. H.; Luo, C. W.; Uen, T. M.; Juang, J. Y.; Lin, J.-Y.; Kobayashi, T.; Yang, H.-D.; Sankar, R.; Chou, F. C.; Berger, H.; Liu, J. M. Phonon Dynamics in Cu x Bi 2 Se 3 (x = 0, 0.1, 0.125) and Bi 2 Se 2 Crystals Studied Using Femtosecond Spectroscopy. *Appl. Phys. Lett.* **2012**, *101* (12), 121912.

(40) Zhang, J.; Peng, Z.; Soni, A.; Zhao, Y.; Xiong, Y.; Peng, B.; Wang, J.; Dresselhaus, M. S.; Xiong, Q. Raman Spectroscopy of Few-Quintuple Layer Topological Insulator Bi 2 Se 3 Nanoplatelets. *Nano Lett.* **2011**, *11* (6), 2407–2414.

(41) Gnezdilov, V.; Pashkevich, Yu. G.; Berger, H.; Pomjakushina, E.; Conder, K.; Lemmens, P. Helical Fluctuations in the Raman Response of the Topological Insulator Bi 2 Se 3. *Phys. Rev. B* **2011**, *84* (19), 195118.

(42) Li, Z.; Zhang, X.; Zhao, X.; Li, J.; Herng, T. S.; Xu, H.; Lin, F.; Lyu, P.; Peng, X.; Yu, W.; Hai, X.; Chen, C.; Yang, H.; Martin, J.; Lu, J.; Luo, X.; Castro Neto, A. H.; Pennycook, S. J.; Ding, J.; Feng, Y.; Lu, J. Imprinting Ferromagnetism and Superconductivity in Single Atomic Layers of Molecular Superlattices. *Adv. Mater.* **2020**, *32* (25), 1907645.

(43) Sharma, M. M.; Sang, L.; Rani, P.; Wang, X. L.; Awana, V. P. S. Bulk Superconductivity Below 6 K in PdBi2Te3 Topological Single Crystal. *J. Supercond Nov Magn* **2020**, *33* (5), 1243–1247.

(44) Biesinger, M. C.; Lau, L. W. M.; Gerson, A. R.; Smart, R. St. C. Resolving Surface Chemical States in XPS Analysis of First Row Transition Metals, Oxides and Hydroxides: Sc, Ti, V, Cu and Zn. *Appl. Surf. Sci.* **2010**, *257* (3), 887–898.